A Blind Ka- and Q- band survey for Molecular Absorption

A thesis submitted towards partial fulfilment of
BS-MS Dual Degree Programme

by

Avani Gowardhan

under the guidance of

Nissim Kanekar

NCRA-TIFR

Indian Institute of Science Education and Research
Pune

Certificate

This is to certify that this thesis entitled "A Blind Ka and Q band survey for Molecular Absorption at high redshift", submitted towards the partial fulfilment of the BS-MS dual degree programme at the Indian Institute of Science Education and Research(IISER) Pune represents original research carried out by Avani Gowardhan at the National Centre for Radio Astrophysics, Tata Institute for Fundamental Research (NCRA-TIFR), under the supervision of Nissim Kanekar during the academic year 2013-2014.

Student
Avani
Gowardhan

Supervisor
Nissim Kanekar

Acknowledgements

This project would not have been possible without the guidance and unfailing patience of my advisor, Dr. Kanekar, which has been sorely tried over the past year.

For making all my years at IISER memorable, I would like to thank all my friends; Purvi, Ankita, Deepika and Sravani. I would like to thank fellow physicists Aashay, Bhavesh, and Rohit, for the many constructive hours spent in their company. I would also like to express sincere gratitude towards all the students at NCRA in the past year, for providing help, encouragement, and food. For challenging and stimulating scientific discussions, I would like to thank Prof. Rajaram Nityananda, Barnali Das and Akash Guru. Finally, I would like to dedicate this thesis to Aditi, for providing warmth and succor at all times.

AVANI GOWARDHAN

Abstract

We have conducted a large-scale "blind" millimetre wavelength survey for redshifted molecular absorption using the CO and HCO^+ rotational transitions. We have observed 549 radio-selected sources in the Ka and Q bands in the frequency range 32- 48 GHz, using the Karl G. Jansky Very Large Array (VLA), covering the redshift range $0.85 < z < 2.60$ and $2.72 < z < 4.57$ with a median redshift of $z = 1.5$. Due to observational issues, only 501 of the total sample of 549 sources were analysed during the course of this project. 245 of these sources have known redshifts, giving us a total redshift path $\Delta z \sim 188.2$ at the 5σ optical depth threshold of $\Delta\tau \leq 0.35$. This sensitivity is sufficient to detect $N_{CO} = 2.8 \times 10^{15}$ cm^{-2} and $N_{HCO^+} = 3.4 \times 10^{12}$ cm^{-2}. Assuming the Galactic CO-to-H_2 and HCO^+-to-H_2 conversion factors, these column densities correspond to H_2 column densities of $N_{H_2} \geq 9.3 \times 10^{20}$ cm^{-2} and $N_{H_2} \geq 1.7 \times 10^{21}$ cm^{-2}. All the currently known redshifted molecular absorbers would be detected at this sensitivity.

Standard statistical tests were used to test the obtained spectra for Gaussianity, and spectra showing non-Gaussian behaviour were excluded from further analysis. In addition, we also excluded several features found at the same observing frequency along multiple sightlines since these are likely to arise due to terrestrial radio frequency interference.

After excluding spectral channels with radio frequency interference RFI and spectra with non-Gaussian behaviour from the sample, we searched the remaining spectra for features with $\geq 5\sigma$ significance. We obtained 36 putative features in absorption, and 17 features in emission at $\geq 5\sigma$ significance, excluding those features found towards PKS1830-211. In all, we have 37 possible absorption systems.

Assuming that the 20 absorption features (with $\geq 5\sigma$ significance) in excess of those detected in emission are real, we obtain a redshift number density of molecular absorbers $n(z) = 0.106^{+0.029}_{-0.024}$ at the median survey redshift of $z = 1.5$. Conversely, assuming that all absorption features with $\geq 5\sigma$ significance except for those towards PKS1830-211 at $z = 0.88582$ arise from systematic effects yields $n(z) = 0.005^{+0.012}_{-0.004}$.

Finally, we have compared the redshift number density of damped Lyman-α absorbers (from the literature) and molecular absorbers (from our survey),to obtain $1.1 \leq n_{\rm DLA}/n_{H_2} \leq 24$. If the atomic and molecular gas are in the form of a rotating disk, as is the case in the local Universe, the ratios of the transverse sizes of the disks are $1.0 \leq s_{\rm HI}/s_{H_2} \leq 4.9$. This is the first comparision between the spatial extents of molecular and atomic gas in high redshift galaxies.

Contents

Chapter 1

Introduction

Molecular gas is one of the most important constituents of the interstellar medium (ISM) in galaxies. It plays a critical role in star formation in galaxies, which in turn is important for galaxy evolution. However, despite its importance in the context of galaxy evolution, the evolution of the molecular content of galaxies with redshift is still not well understood. In this study, we aim to study the abundance and evolution of molecular absorption as a function of redshift.

1.1 Molecules in the ISM

Molecular clouds are cold and dense regions in the ISM, typically having temperatures $\sim 10-100$ K, and are primarily composed of molecular hydrogen. For example, in the Milky Way, they contribute only 1-2% of the volume, while accounting for roughly half the mass in the interstellar medium. The low temperatures and high densities facilitate gravitational collapse, which is the first step leading to star formation. They also contain large amounts of dust, which obscure most of the radiation in the optical and the ultraviolet from background sources. Since dust is transparent at the radio and millimetre wavelengths, it might be expected that we could study these systems at those frequencies using molecular rotational transitions. However, H_2 is a homonuclear diatomic molecule, with a permanent dipole moment of zero, and its lowest energy transitions are quadrupole transitions, which require an excitation temperature of ~ 500 K or more, and have low Einstein A coefficients. The H_2 rotational/vibrational transitions are therefore not excited in the ISM, except in rare starburst conditions. It is extremely difficult to detect directly. It has been observed via electronic transitions in the optical or the ultraviolet, but only in cases of sightlines with low dust content. The bulk of the molecular gas in the Universe is thus, to all practical purposes, invisible to us.

However, the presence of molecular gas along a sightline can be identified

using "tracers" such as CO or HCO^+, which are abundantly found in molecular clouds. Because of their low dipole moments and high Einstein A coefficients, the rotational levels of these molecules are easily excited, even at the low temperatures of ~ 10 K.

Empirical relations have been found between the CO and H_2 column densities, as well as between the HCO^+ and H_2 column densities, in the Milky Way (e.g. Liszt & Lucas, 2000a; Burgh et al., 2007). The CO to H_2 conversion factor has been found to depend on the type of molecular cloud (i.e. diffuse or dense gas), with $N_{\rm CO}/N_{\rm H_2} = 3 \times 10^{-6}$ (e.g. Burgh et al., 2007). Conversely, the HCO^+ to H_2 conversion factor appears to be more universal, with $N_{\rm HCO^+}/N_{\rm H_2} = 2 \times 10^{-9}$ (Liszt & Lucas, 2000a). While it is known that the CO-to-H_2 conversion factor depends on local conditions, including metallicity, density, size, etc, we will use a single conversion factor, $N_{\rm CO}/N_{\rm H_2} = 3 \times 10^{-6}$ in this thesis, assuming that this is valid at high redshifts.

Molecular gas can be studied in both absorption and emission. However, absorption and emission studies are sensitive to different physical conditions; absorption studies are more sensitive to excitationally cold molecular gas, which is likely to be the state for the bulk of the molecular component in quiescent galaxies, whereas emission studies probe molecular gas of higher excitation temperatures. For an emission line, the quantity measured is the velocity integrated line intensity,

$$\int T_A dV = (\Omega)^{-1}(1+z)^3 {D_L}^{-2} \Delta V T_{ex} \tag{1.1}$$

where Ω is the beam-filling factor, ΔV is the velocity width of the profile, D_L is the luminosity distance, T_A is the line intensity, and T_{ex} is the excitation temperature. The measured quantity for an absorption line is the velocity integrated optical depth, which is given by,

$$\int \tau_v dv = \frac{N_{tot}}{T_{ex}} \mu_0^2 (1 - \exp(-\frac{h\nu}{kT_{ex}})) = \frac{N_{tot}}{T_{ex}^2} \mu_0^2 \tag{1.2}$$

where τ_v is the optical depth, dv is the line width in velocity units, μ_0 is the permanent dipole moment of the transition, and N_{tot} is the total column density of the gas. It can be seen that the velocity integrated line intensity *increases* with the excitation temperature, whereas the velocity integrated optical depth varies as $1/T_{ex}^2$. Thus, absorption studies are more sensitive to gas with lower excitation temperatures, whereas emission studies are sensitive to molecular gas at high temperatures, e.g. in starburst galaxies. When the excitation is dominated by collisional processes, higher excitation temperatures correspond to denser gas, and lower temperatures to more diffuse gas.

The sensitivity of absorption studies is limited only by the flux density of the background source, and is thus independent of the distance of the absorbing

material. This makes absorption a better tool for studying normal galaxies at high redshifts. For emission studies, the line intensity decreases with increasing redshift, so that only the brightest sources can be detected at the highest redshifts. Many emission studies of molecular gas using CO transitions have been conducted, focusing mainly on massive and highly luminous objects, e.g. dusty starburst galaxies bright in the sub-mm, and on highly lensed systems at high redshifts (Carilli & Walter, 2013; Riechers et al., 2010). This implies that we are unlikely to see "typica" galaxies in emission. Emission studies also obtain the global properties of the molecular gas, such as the total gas content, the rotational velocity etc, whereas absorption studies probe properties on a much smaller scale; they probe a thin pencil beam through the absorber, and the spatial resolution is limited only by the extent of the background source. Since molecular absorption is more sensitive than emission at high redshifts, we can detect a far greater number of molecules. This makes it possible to study and compare the evolution of multiple molecular species over a large redshift range. So far more than 30 molecules have been detected in absorption at high redshifts, whereas fewer than 10 have been seen in emission (e.g. Muller et al., 2011).

1.2 Molecular absorption studies

Molecular absorption is an extremely powerful tool for studying "typical" galaxies at cosmological distances. Studies of the evolution of molecular absorption with redshift can provide information on the gas available for star formation at different epochs. Such studies can also yield information on the evolution of quantities such as the cosmological mass density of molecular hydrogen with redshift. Similar studies have been performed for neutral atomic gas using samples of damped Lyman-α systems (DLAs) via optical spectroscopy (Wolfe et al., 1986).We could probe the redshift evolution of molecular chemistry and isotopic abundances, due to the large number of available molecular transitions. Such studies of redshifted absorbers may allow the detection of molecules such as H_2O and O_2, which cannot be observed in the local Universe due to atmospheric absorption at the line frequencies. Even surveys tracing molecular abundances over different epochs would be possible (Muller et al., 2011). The large number of transitions at different epochs can be used to probe changes in fundamental constants (Kanekar, 2011; Drinkwater et al., 1998). If the excitation is dominated by the Cosmic Microwave Background (CMB) radiation, such as for the different transitions of H_3CN, we can constrain the CMB temperature at different redshifts (e.g. Muller et al., 2013). Since the molecular gas distribution within a galaxy is less extended as compared to atomic hydrogen, lines of sight showing absorption features will have a small impact factor, increasing the probability of gravitational lensing. Indeed, of the

five systems known to date, three are gravitationally lensed systems, and the other two show absorption by gas in the active nucleus environment. In the cases where absorption takes place in a gravitationally lensed system, time-delay studies can be used to estimate the Hubble's constant.

The present major hindrance in these kind of studies is the lack of known molecular absorbers at high redshift. Despite numerous targeted searches, only five molecular absorbers are known to date, all at $z < 0.9$ (Wiklind & Combes, 1994; Wiklind & Combes, 1996a, 1995, 1996b; Kanekar et al., 2005). This dearth of systems is the main motivation for this project, where we search for molecular absorbers over a large redshift range, from $0.85 < z < 2.6$ and from $2.72 < z < 4.57$.

1.3 Known Molecular absorption systems

SOURCE	z_e	z_a	N_{CO} (cm^{-2})	N_{H_2} (cm^{-2})
PKS1413+135	0.247	0.247	2.3×10^{16}	4.0×10^{20}
B1504+377	0.673	0.673	6.0×10^{16}	1.2×10^{21}
B0218+357	0.94	0.685	2.0×10^{19}	4.0×10^{23}
PMN J0134-0931	2.22	0.765	–	–
PKS1830-211	2.51	0.885	2.0×10^{18}	4.0×10^{22}

Table 1.1: For all the currently known molecular absorbers at high redshifts, the background source redshift z_e, the redshift of absorption z_a, the CO column density N_{CO}, and the H_2 column density N_{H_2} have been shown.

Only five molecular absorption systems are known to date : PKS 1413+135 (Wiklind & Combes, 1994) and B1504+377 (Wiklind & Combes, 1996a), which show absorption by gas in the active nucleus environment, and PKS 1830-211 (Wiklind & Combes, 1996b), B0218+357 (Wiklind & Combes, 1995), and PMN J0134-0931 (Kanekar et al., 2005), where the absorption arises in an intervening spiral gravitational lens. Their properties have been summarised in Table 1.1.

PKS 1413+135: This was the first system at cosmological distances where molecular absorption was detected. The background source PKS1413+135 is at a redshift of $z = 0.247$ (Wiklind & Combes, 1994), and located within

the galaxy where the absorption is taking place. This was initially observed because HI 21 cm absorption had been detected at $z \sim 0.247$ towards this object (Carilli et al., 1992); searches for molecular absorption were hence carried out at the redshift of the strong HI 21cm absorption.. Since then, a number of molecular lines including CO, HCO^+, OH, & HCN (Kanekar & Chengalur, 2002; Wiklind & Combes, 1997) have been detected in this system. This is one of the few systems to show conjugate OH transitions, which is important for fundamental constant evolution studies (Kanekar et al., 2004). The host galaxy is a highly inclined disk galaxy, and the CO absorption profile is the narrowest known, with a full width at half maximum of ~ 2 km/s..

B1504+377: The quasar B1504+377 is a radio loud AGN hosted by a edge-on disc galaxy at a redshift of $z = 0.672$. The initial observations revealed at least seven molecular transitions (Wiklind & Combes, 1996a); this system was found in a survey targeting 50 sources, towards which absorption had been detected in other species. HI 21-cm (Carilli et al., 1997) and OH 1667/1665 MHz lines lines (Kanekar & Chengalur, 2002) have also been detected.

This system contains absorption at two nearby redshifts, $z = 0.67335$ and $z = 0.67150$, with a velocity separation of 330 km/s. The two components were interpreted as coming from a spiral arm and a nuclear ring undergoing non-circular motion (Wiklind & Combes, 1996a), as it is difficult to produce two absorption components at very different velocities if the absorbing gas is in pure rotational motion. However, more recent HI 21cm absorption studies have shown that the two absorbers arise from outflowing gas, extending from the AGN redshift, $z = 0.674$ all the way down to $z = 0.670$ (Kanekar & Chengalur, 2008).

B0218+357 This is a gravitationally lensed system, with the absorbing galaxy at $z = 0.685$ and the background source at $z = 0.94$, and was observed as part of a sample comprised of sources, towards which HI 21 cm absorption had been seen and which were also gravitational lenses (Wiklind & Combes, 1995). The lensing galaxy is almost face-on; in the lensed image, the source is split into two main images. High resolution very long baseline interferometry images show two bright spots in each of the two images, referred to as the A and B components. The lines of the isotopic variants, ^{13}CO and $C^{18}O$ are optically thick, so only lower limits on the column densities are obtained, though $C^{17}O$ has not been detected. This has the largest molecular hydrogen column density amongst all the currently known absorbers, $N_{H_2} = 4 \times 10^{23}$ cm^{-2}. Molecular species such as NH_3, H_2O and LiH have been found;

it was also searched for O_2, but only upper limits could be deduced (e.g. Combes & Wiklind, 1997; Combes et al., 1997).

The continuum level does not go to zero in transitions that are expected to be optically thick, and that appear saturated in the observed spectra, indicating that the absorbing gas covers only one of the components, A, but that this gas is optically thick. Since it is optically thick, the A component might be expected to be obscured in the optical. However, it was found that a significant part of A was obscured, while a small part remains unobscured. Since the optical emission is over a small spatial region, it implies large density variations in the molecular gas over small distance scales. Monitoring the time delay, taken together with a lensing model that takes into account the spiral arms, the Hubble's constant was estimated to be $H_0 = 70$ km $\mathrm{Mpc}^{-1}\mathrm{s}^{-1}$ (York et al., 2005).

J0134-0931 This absorber was first detected in HI 21cm absorption and later in OH absorption as well as emission (Kanekar & Briggs, 2003; Kanekar et al., 2005). On searching for other molecular lines, however, only upper limits for N_{CO} and N_{HCO^+} lines were obtained, whereas the strongest molecular lines have been detected in all other OH absorbers at high redshifts. This is also a gravitationally lensed system, with the lensing galaxy at $z = 0.7645$ and the background quasar at $z = 2.22$(Winn et al., 2002). There are seen to be 6 lensed images in a high resolution image of the lensing galaxy(Winn et al., 2003). All four 18 cm OH lines have been detected here, including conjugate OH lines, which have been seen only in one other redshifted absorber(Kanekar et al., 2005). This is the most distant as well as the brightest OH megamaser known to date.

PKS1830-211 This the most distant radio molecular absorber known, with the absorbing galaxy at $z = 0.88582$. This is the only system to have been detected in a blind survey(Wiklind & Combes, 1996b). It is a gravitationally lensed system, consisting of two images, each containing a core and a jet-like feature along with an Einstein ring. The two images are referred to as the NE and SW components, and most of the absorption is in front of the SW component. Molecular absorption is detected for both the images, located one arcsecond apart on the north-east and south-west side, respectively, of the Einstein ring (Wiklind & Combes, 1996b; Muller et al., 2011). The two lines of sight intersect the disk of the $z = 0.89$ galaxy on either side of the central bulge, at galactic distances of $\sim$ 2 kpc (to the SW) and $\sim$ 4 kpc (to the NE).

This molecular gas system has the largest number of detected molecules so far apart from the Milky Way; a total of 28 molecules have been detected

here (Muller et al., 2011), with another 8 isotopic variants. The presence of isotopic variants such as ^{13}CO and ^{18}CO implies that the gas is optically thick. However, the continuum flux does not go to zero, implying that only part of the continuum source is covered by the obscuring molecular gas, and that this gas is optically thick.

1.4 Blind Radio Absorption surveys

The extreme paucity of known molecular absorption systems despite numerous targeted searches (Murphy et al., 2001; Wiklind & Combes, 1995; Drinkwater et al., 1998)can be attributed to a multitude of reasons. The most important of these is the bias introduced due to optical selection of background targets for absorption searches. Since the redshift determination typically uses transitions in the optical or the ultraviolet, which requires the target source to be unobscured by dust, selection on the basis of optical redshifts implicitly biases the sample towards sightlines with low dust content, which are less likely to show absorption. Searches at optical frequencies have mostly targeted the ultraviolet H_2 lines in known damped Lyman-α systems (DLAs); in all detections, H_2 fractions were extremely low, $f = 2N_{H_2}/[2N_{H_2} + N_{HI}] \sim 10^{-6} - 0.1$ (Ledoux et al., 2003; Noterdaeme et al., 2008).

This is unsurprising, since the searches targetted quasars that are not highly obscured in the optical, implying low dust content along the sightline. Since high H_2 column densities are typically accompanied by obscuring dust, the lack of dust obscuration implies a low H_2 column density.

Radio and mm-wavelength surveys attempted to circumvent this by searching for millimetre-wave band absorption in reddened radio sources, which are likely to be dusty, but only upper limits for column densities were obtained.Murphy et al. (2003) observed four objects that were strong at millimetre wavelengths but optically faint, with the redshift coverage complete up to $z_{abs} \sim 5$. Even though no confirmed absorption features were found, they demonstrated the importance of wide bandwidth studies, and suggested that with a much larger number of target sources, millimetre-wavelength absorption systems were likely to be discovered.

The first blind survey was conducted by Wiklind & Combes (1996b), and detected the absorber at $z = 0.88582$ towards PKS1830-211. The first large-scale blind search for millimetre wave absorption was conducted by Kanekar et al. (2014) using the Green Bank Telescope. Though no absorp-

tion systems were detected, it showed the feasibility of such surveys. Therefore, we are conducting a blind survey, using a larger radio-selected sample, which includes sources regardless of whether or not their redshifts are known, ensuring that there is no bias against dust-obscured sources.

1.4.1 Redshift Path

An important characteristic of any absorption survey is the redshift path covered Δz, at some optical depth sensitivity τ. This is defined as

$$\Delta z = \int_0^{z_0} g(z) dz \tag{1.3}$$

where $g(z)$ is the redshift path density, and z_0 is the redshift of the background source, such that $g(z)dz$ gives the number of sightlines for which optical depths greater than τ would have been detected in the redshifts from z to $z + dz$ (Lanzetta et al., 1991). The aim of any survey is to maximise its redshift path coverage. It can be shown that the redshift path increases rapidly with the fractional bandwidth; if we have a bandwidth of $\Delta\nu$ around a central frequency of ν, a transition with a rest frame frequency of ν_0 can be observed at a redshift

$$z = \frac{\nu_0}{\nu} - 1 \tag{1.4}$$

And the redshift path covered would be

$$\Delta z = \frac{\nu_0}{\nu - \Delta\nu/2} - \frac{\nu_0}{\nu + \Delta\nu/2} \tag{1.5}$$

$$\Delta z = \frac{\nu_0}{\nu} \frac{\delta}{1 - (\delta/2)^2} \tag{1.6}$$

where $\delta = \frac{\Delta\nu}{\nu}$. It can be seen that the redshift path increases faster than linearly with the fractional bandwidth.

The lack of a sufficiently large fractional bandwidth has been the largest hurdle for radio absorption surveys till now. For example, in the optical, the typical observing band of $4000 - 7000$ Å corresponds to the redshift range $2.3 < z < 4.75$ for the Lyman-α line, which is a redshift path of $\Delta z = 2.45$. On the other hand, the 32 MHz GMRT bandwidth at 610 MHz corresponds to the redshift range $1.21 < z < 1.33$ for the HI 21cm line, which

is a redshift path $\Delta z = 0.12$. Surveys for atomic hydrogen absorption are hence best conducted at optical wavebands. Unfortunately, dust bias issues imply that we can't conduct surveys for molecular absorbers in the optical with H_2 lines; instead, we are forced to work at millimetre wavelengths with rotational lines. Until recently the fractional bandwidth of the best high-frequency radio telescopes, e.g. the Very Large Array, was extremely small, < 0.001, but it is significantly larger with the upgraded Karl G. Jansky Very Large Array (VLA) and the Green Bank Telescope.

1.4.2 Possible transitions

The best lines for a molecular absorption survey are the strongest radio lines, which are the rotational transitions of CO and HCO^+. Different CO and HCO^+ transitions give different overlapping redshift ranges. For example, an observing frequency of 40 GHz corresponds to redshifts $z \approx 1.22$ (HCO^+1-0), $z \approx 1.88$ (CO 1-0), $z \approx 3.46$ (HCO^+2-1), $z \approx 4.76$ (CO 2-1), etc. We can hence choose a frequency range for an absorption survey so as to maximize the redshift coverage towards a target source. As shown by Kanekar et al. (2014), the most suitable frequency range is $31 - 49$ GHz. This would be sensitive to absorption from $0.82 < z < 1.88$ for HCO^+(1-0), $1.35 < z < 2.72$ for CO(1-0), $2.64 < z < 4.75$ for HCO^+(2-1), $3.70 < z < 6.44$ for CO(2-1) i.e - this would cover *all* redshifts $z > 0.82$.

Chapter 2

Background

2.1 Molecular absorbers : A Physical Picture

In order to understand the interactions between the molecules, and between the molecules and the ambient radiation field, we can use the equations of radiative transfer. Let us consider a two energy-level system, where molecules can occupy two discrete energy levels 1 and 2, where $E_2 > E_1$. In the presence of a radiation field, there are three processes that can take place,

Spontaneous emission – A molecule jumps from level 2 to level 1 by spontaneously emitting a photon with energy $h\nu_0 = E_2 - E_1$

Stimulated emission – In the presence of a radiation field, molecules can jump from level 2 to level 1, while emitting a photon of frequency ν_0, such that $E_2 - E_1 = h\nu_0$,

Stimulated absorption – In the presence of a radiation field, molecules can go from level 1 to level 2 after absorbing a photon of frequency ν_0, such that $E_2 - E_1 = h\nu_0$,

Both stimulated emission and absorption depend on the presence of a radiation field containing photons with the correct energy and polarization. The probabilities for each process per unit volume are written in the form of the Einstein coefficients, A_{21}, B_{12} and B_{21}, such that if there are N_1 molecules in state 1 and N_2 molecules in state 2, the rate of molecules undergoing stimulated emission is $N_2 B_{21}$ and so on. Since the energies E_1 and E_2 have a finite spread, the energy $E_2 - E_1$ will not be a unique value. In frequency units, we can say that the emission line can be described by a line profile that will be sharply peaked at some frequency ν_0 and normalised such that

$$\int_0^\infty \phi(\nu)d\nu = 1 \tag{2.1}$$

where the $\phi(\nu)$ is the function representing the normalised line profile. If the intensity of the radiation field is given by I_ν, we can define an average intensity by

$$\bar{I} = \int_0^\infty I_\nu \phi(\nu)d\nu \tag{2.2}$$

The average energy density in the radiation field can be written as

$$\bar{U} = \frac{4\pi\bar{I}}{c} \tag{2.3}$$

If the system is at equilibrium, the number of atoms in each state must be constant, which implies that

$$N_1 B_{12}\bar{U} = N_2 B_{21}\bar{U} + N_2 A_{21} \tag{2.4}$$

For a system in thermodynamic equilibrium, the number of atoms in different energy states is related by the equation

$$\frac{N_2}{N_1} = \frac{g_2}{g_1}\exp(-\frac{h\nu_0}{kT}) \tag{2.5}$$

where g_1 and g_2 are the statistical weights of the two energy states, and T is the temperature of the cavity in Kelvins. From (2.4), we can write the average energy density of the radiation field as

$$\bar{U} = \frac{A_{21}}{\frac{N_1}{N_2}B_{12} - B_{21}} \tag{2.6}$$

From this and (2.5) we have,

$$\bar{U} = \frac{A_{21}}{\frac{g_1}{g_2}\exp(\frac{h\nu_0}{kT})B_{12} - B_{21}} \tag{2.7}$$

But in thermodynamic equilibrium (hereafter referred to as TE), we know that the energy density must be given by the Planck equation

$$\bar{U} = \frac{4\pi B_\nu(T)}{c} = \frac{8\pi\nu^3}{c^3}\frac{1}{\exp(\frac{h\nu_0}{kT}) - 1} \tag{2.8}$$

Since the equations (2.6) and (2.8) should be identical, we get

$$g_1 B_{12} = g_2 B_{21} \tag{2.9}$$

$$A_{21} = \frac{8\pi h\nu^3}{c^3} B_{12} \tag{2.10}$$

This can be extended for use in non-TE conditions, since no knowledge is needed about the thermodynamic properties of the cavity.

For light of specific intensity I_ν passing through a slab of thickness ds, the change in the specific intensity can be written as

$$dI = -\kappa_\nu I_\nu ds + \epsilon_\nu ds \tag{2.11}$$

where κ_ν is the absorptivity, and ϵ_ν is the emissivity of the material. Each of the three processes – stimulated emission, absorption, and spontaneous emission – contribute to the net change in the energy, and the equations for each are

$$dE^1(\nu) = h\nu_0 N_2 A_{21} \phi_e(\nu) dV \frac{d\Omega}{4\pi} d\nu dt \tag{2.12}$$

Similarly, we get the following equations for the total energy absorbed,

$$dE^2(\nu) = h\nu_0 N_1 B_{12} I_\nu \phi_{sa}(\nu) dV \frac{d\Omega}{4\pi} d\nu dt \tag{2.13}$$

And the energy released due to stimulated emission is

$$dE^3(\nu) = h\nu_0 N_2 B_{21} I_\nu \phi_{se}(\nu) dV \frac{d\Omega}{4\pi} d\nu dt \tag{2.14}$$

where dV is the volume element, $d\Omega$ is the solid angle over which the energy is released, dt is the time interval in which the energy is released, and $d\nu$ is the infinitesimal bandwidth.

Assuming the same line profiles for absorption and emission, we put $\phi_e = \phi_{sa} = \phi_{se} = \phi$. We know that

$$\begin{aligned} dE^1(\nu) + dE^3(\nu) - dE^2(\nu) &= dI d\nu ds d\sigma dt d\Omega \\ &= \frac{h\nu_0}{4\pi}[N_2 A_{21} + N_2 B_{21} \frac{4\pi}{c} I_\nu - N_1 B_{12} \frac{4\pi}{c} I_\nu]\phi(\nu) d\nu ds d\sigma dt d\Omega \end{aligned} \tag{2.15}$$

$$\Rightarrow \frac{dI}{ds} = -\frac{h\nu_0}{c}(N_1 B_{12} - N_2 B_{21}) I_\nu \phi(\nu) + \frac{h\nu_0}{4\pi} N_2 A_{21} \phi(\nu) \tag{2.16}$$

Comparing this with equations (2.11), we get following relations

$$\kappa(\nu) = \frac{h\nu_0}{c} N_1 B_{12} (1 - \frac{g_1 N_2}{g_2 N_1}) \phi(\nu) \tag{2.17}$$

and

$$\epsilon(\nu) = \frac{h\nu_0}{4\pi} N_2 A_{21} \phi(\nu) \tag{2.18}$$

From (2.17) and (2.18) we find that

$$\frac{\epsilon(\nu)}{\kappa(\nu)} = \frac{2h\nu^3}{c^2} (\frac{g_2 N_1}{g_1 N_2} - 1)^{-1} \tag{2.19}$$

But we know that for Local thermodynamic Equilibrium, this should be equal to the Planck function, resulting in

$$\frac{N_2}{N_1} = \frac{g_2}{g_1} \exp(-\frac{h\nu_0}{kT}) \tag{2.20}$$

Then the absorption coefficient becomes,

$$\kappa_\nu = \frac{c^2}{8\pi} \frac{1}{\nu_0^2} \frac{g_1}{g_2} N_1 A_{21} (1 - \exp(-\frac{h\nu_0}{kT})) \phi(\nu) \tag{2.21}$$

where we have replaced the B coefficient by the A coefficient, using

$$B_{12} = \frac{g_1}{g_2} A_{21} \frac{c^3}{8\pi h\nu^3} \tag{2.22}$$

If the transitions are rotational transitions of molecules, then the dipole transition probabilities are given as

$$A_{mn} = \frac{64\pi^4}{3hc^3} \nu_{mn}^3 |\mu_{mn}|^2 \tag{2.23}$$

where m and n are the two states, and μ_{mn} is the average dipole moment for this transition. If we assume that the gas is cool, where only the two lowest states are populated to a significant extent, and that collisions can excite molecules from one state to another, and that they, along with radiation, govern the transition rate, we can modify (2.4) to write

$$N_1 (C_{12} + B_{12} \bar{U}) = N_{2(} B_{21} \bar{U} + A_{21} + C_{21}) \tag{2.24}$$

where C_{ij} is the probability of a transition from state i to state j occurring per particle per second (in $cm^3 s^{-1}$)

$$C_{ik} = N_i \int_0^\infty \sigma_{ik} v f(v) dv \tag{2.25}$$

where σ_{ik} is the collision cross section, and $f(v)$ the velocity distribution of the colliding particles. If collisions dominate, the principle of detailed balance leads to

$$\frac{C_{12}}{C_{21}} = \frac{N_2}{N_1} = \frac{g_2}{g_1}\exp(\frac{-h\nu_0}{kT_K}) \tag{2.26}$$

where T_K is the kinetic temperature. Substituting (2.26) and (2.20) into (2.24), we get

$$\frac{N_2 g_1}{N_1 g_2} = \exp(\frac{-h\nu_0}{kT_{ex}}) = \exp(\frac{-h\nu_0}{kT})\frac{A_{21} + C_{21}\exp(\frac{-h\nu_0}{kT_K})[\exp(\frac{h\nu_0}{kT}) - 1]}{A_{21} + C_{21}[\exp(\frac{h\nu_0}{kT}) - 1]} \tag{2.27}$$

where we characterise $\frac{N_1}{N_2}$ by the excitation temperature,

$$\frac{N_2}{N_1} = \frac{g_2}{g_1}\exp(\frac{-h\nu_0}{kT_{ex}}) \tag{2.28}$$

The excitation temperature is a function of both the radiation temperature T and the kinetic temperature T_K. If radiation dominates the equation ($C_{21} \ll A_{21}$), then $T_{ex} \to T$, and if collisions dominate ($C_{12} \gg A_{21}$) then $T_{ex} \to T_K$. Since C_{ik} increases with increasing N, collisions will dominate in high density situations, and then $T_{ex} \to T_K$. The other case will hold true in the low density situation.

The above equations will give us the absorption coefficient in frequency units; to get it in terms of the corresponding Doppler velocities,

$$\frac{\nu_0 - \nu}{\nu_0} = \frac{v}{c} \tag{2.29}$$

$$d\tau(\frac{v}{kms^{-1}}) = -\kappa_\nu d\frac{s}{cm} = \frac{c^2}{8\pi}\frac{1}{\nu_0^2}\frac{g_1}{g_2}N_1 A_{21}(1 - \exp(-\frac{h\nu_0}{kT}))\phi(\nu)d\frac{s}{cm} \tag{2.30}$$

Integrating over both v and s ,

$$\int_{-\infty}^{\infty}\tau(v)dv = \iint \kappa(v)dvds = -\frac{c^2}{8\pi}\frac{1}{\nu_0^2}\frac{g_1}{g_2}A_{21}(1 - \exp(-\frac{h\nu_0}{kT}))\mathscr{N}_1\int_{-\infty}^{\infty}\phi(v)dv \tag{2.31}$$

where $\mathscr{N}_1 = \int_0^\infty N_1 ds$ is the column density of the gas in the first energy state.

$$\int_{-\infty}^{\infty}\tau(v)dv = -\frac{c^2}{8\pi}\frac{1}{\nu_0^2}\frac{g_1}{g_2}A_{21}(1 - \exp(-\frac{h\nu_0}{kT}))\mathscr{N}_1 \tag{2.32}$$

$$\mathscr{N}_1 = -\frac{8\pi}{c^2}\frac{\nu_0^2 g_1 \int_{-\infty}^{\infty}\tau(v)dv}{g_2 A_{21}(1-\exp(-\frac{h\nu_0}{kT}))} \tag{2.33}$$

This is the column density for a particular level. If the total column density is $\mathscr{N}_{tot}$,

$$\frac{\mathscr{N}_1}{\mathscr{N}_{tot}} = \frac{2J+1}{\mathscr{Z}}\exp(-\frac{hB_eJ(J+1)}{kT}) \tag{2.34}$$

where $\mathscr{Z}$ is the partition function, and

$$\mathscr{Z} = \sum_{J=0}^{\infty}(2J+1)\exp(-\frac{hB_eJ(J+1)}{kT}) \tag{2.35}$$

If $hB_e \ll kT$,

$$\mathscr{Z} = \int(2J+1)\exp(-\frac{hB_eJ(J+1)}{kT})dJ = \frac{kT}{hB_e}, \tag{2.36}$$

Finally, for the (1-0) transition, we have

$$\mathscr{N}_{tot} = -\frac{8\pi}{c^2}\frac{\nu_0^2 \int_{-\infty}^{\infty}\tau(v)dv}{A_{21}(1-\exp(-\frac{h\nu_0}{kT}))} \tag{2.37}$$

So, given a absorption line in doppler-shifted velocity units, we can calculate $\int_{-\infty}^{\infty}\tau(v)dv$, assuming $T_{ex} = 10K$. Using the above equation, we can then estimate the column density of the molecular species in question in the absorber.

Chapter 3

A VLA Survey for radio molecular absorption

A large number of surveys have been carried out at optical wavelengths for damped Lyman-α absorbers (DLAs; e.g. Wolfe et al., 2005). These have been used to measure the cosmological mass density in neutral atomic gas, as well as the probability of detecting Lyman-α absorption as a function of redshift i.e. the number density of DLAs as a function of redshift (Wolfe et al., 2005). Optical surveys typically target bright quasars with known redshifts; it is then easy to get high sensitivity absorption spectra. But these are biased towards sightlines without dust, since any background quasar would be obscured by dust and therefore would not be seen. Molecular gas is typically found with large amounts of dust along the sightline, making it difficult to see a background quasar in the optical. Therefore, we are conducting a blind absorption survey using a complete radio-selected sample of background targets in order to detect absorbers with high dust content. "Blind" implies that we are not biased by optical selection of the background targets. Radio flux densities are unaffected by dust in a foreground absorber, and radio-selected samples are thus not biased by dust extinction.

3.1 Lines targeted by the survey

The best transitions for a blind search in molecular absorption are the strongest radio lines, amongst which are the rotational transitions of CO (115 GHz, 230 GHz, 345 GHz ...) and HCO^+ (89 GHz, 178 GHz, 267 GHz ...). Millimetre-wavelength CO/HCO^+ rotation lines are strong lines, with relatively high Einstein A-coefficients, and thus easily detectable for high H_2 column densities. The column densities of CO are typically 1000 times higher than that of HCO^+, and their respective Einstein A coefficients are such that low HCO^+ column densities produce

lines of optical depth comparable to those produced by higher CO column densities. Specifically, $A_{10}(HCO^+) = 4.2\times10^{-5}$ s^{-1} and $A_{10}(CO) = 7.4\times10^{-8}$ s^{-1}, while their conversion factors to H_2 are $N_{HCO+}/N_{H2} = 2\times10^{-9}$ and $N_{CO}/N_{H2} = 3\times10^{-6}$ (Liszt & Lucas, 2000a; Burgh et al., 2007), so that for a given H_2 column density their optical depths are comparable. Therefore, we can cover different redshift ranges for each of these transitions, having similar sensitivities to the H_2 column density. The same holds true for the HCO^+ (2-1) and CO(2-1) lines.

As mentioned in Chapter 1, the frequency coverage from 31 to 49 GHz provides complete redshift coverage from $z \geq 0.82$. However, we have chosen to observe from 32-48 GHz because including the entire frequency range from 31-49 GHz would have required two extra frequency settings, and doubled the observing time, for a relatively small increase in bandwidth. Therefore we have observed only in the redshift range 32-48 GHz; this covers the redshift range $0.85 < z < 2.6$, and $2.72 < z < 4.57$. A similar study has earlier been attempted with the GBT, covering a narrower frequency range from 40-49.5 GHz (Kanekar et al., 2014).

3.2 Observations

We chose to use the Karl G. Jansky Very Large Array for the molecular absorption survey due to its uniform frequency coverage above 1 GHz and the excellent WIDAR correlator. The frequency range 31-49 GHz can be covered at the VLA by the Ka-band (26-40 GHz) and Q-band (40-49 GHz) receivers. Further, the new 3-bit WIDAR samplers had just been released at the time of our proposed observations, allowing us to use a large instantaneous bandwidth of 8.192 GHz. This meant that we could cover a total bandwidth of $\sim$ 16 GHz with two settings, from 32-48 GHz. We have bandwidths of 8.192 GHz in both the Ka and Q bands, from 32 GHz to 40 GHz, and from 40 GHZ to 48 GHz. The 8 GHz bandwidths are divided into 4 IF bands, each of which is divided into 16 digital sub-bands, giving us a total of 64 sub-bands in all. We have chosen to use 128 channels in each of these 64 sub-bands; in all, there are 8192 channels, with a spectral resolution of 1 MHz, which corresponds to a velocity resolution of 6.2 km/s at 48 GHz and to 9.4 km/s at 32 GHz. The number of channels in each sub-band was chosen so as to achieve the above velocity resolution, sufficient for detecting narrow absorption lines. This was designed for the absorption survey. The large instantaneous bandwidth combined with the high spectral resolution implied a high data rate and large data volumes. A typical 3-hour observing run produced 150 GB of data in the basic format, which swelled to $>$ 200 GB on conversion into the analysis format.

3.3 Target sample

The sample selection is a critical aspect of the survey. The three most important considerations while selecting the target source sample are

(i) It should be a complete radio sample. Unfortunately there's no uniform all-sky high-frequency survey available from which one might select the targets, and so we chose to use two surveys, one in the northern sky, and one in the southern. We have selected target sources from the AT20G survey, a blind Australa Telescope Compact Array survey at 20 GHz, of the entire sky south of declination 0. The AT20G survey is complete to a flux density of 100 mJy (Murphy et al., 2010). For the northern sky, we used sources from the Kuhr 5 GHz sample, which is complete at 5 GHz to a flux density of 1 Jy (Kühr et al., 1981).

(ii) The target sources should be bright, so that good optical depth limits can be obtained. We therefore used a uniform flux density threshold of 100 mJy at 40 GHz, assuming a typical spectral index of $\alpha - 0.8$ for all sources.

(iii) Since the redshift path is one of the defining parameters for an absorption survey, we aimed to get as large a redshift path as possible, i.e. as many sources as possible, and at high redshifts. Therefore we have included sources with known redshifts $z \geq 1$, so as to get a minimum $\Delta z = 0.15$ for every source.

Finally, we have also included sources *without* measured redshifts, so as to avoid bias against targets obscured by dust and thus without optical redshifts. The final sample consists of 585 targets, from the AT20G sample and from the 1 Jy Kuhr et al. sample. We have 288 sources with known redshifts ($z \geq 1$), and 297 sources without known redshifts.

3.4 Redshift Path

We are targetting absorption lines with rest frequencies of 115.271 GHz (CO 1-0), 89.188 GHz (HCO^+ 1-0), and 178.376 GHz (HCO^+ 2-1), at observing frequencies from 32 GHz to 48 GHz. This corresponds to a redshift range of $0.9 < z < 1.8$ for the HCO^+(1-0) line, $1.4 < z < 2.6$ for the CO(1-0) line, and $2.7 < z < 4.6$ for the HCO^+(2-1) line. We will compute the redshift path using the equation (1.3). The redshift path can also be written as

$$\Delta z = \sum_{i=0}^{N} dz_i \tag{3.1}$$

Since we are finally covering the redshift ranges of $0.9 < z < 2.6$ and $2.7 < z < 4.6$, the redshift path contributed by a source at a redshift of $z = 1$ would be $\Delta z = z - 0.85 = 0.15$, by a source at a redshift of $z = 1.6$ would be $\Delta z = 0.75$, and for a source with redshift of $2.6 < z < 2.7$ would be $\Delta z = 1.75$ and so on. The

CO(2-1) line corresponds to a very high redshift range for our frequency coverage, higher than the highest redshift of our target sample. However, it's possible that some of the sources without known redshifts might be at $z > 4.57$ and those would be picked up in the CO (2-1) line. It therefore does not contribute to the redshift path, but is still useful.

We have a total of 585 sources, of which 288 have known redshifts and 297 do not. The total expected redshift path for the survey, considering all three transitions, is $\Delta z \approx 236.3$.

3.5 Sensitivity

We have set our target root-mean-square (RMS) noise to 6.6 mJy per 10 km/s channel, which corresponds to an optical depth RMS noise of $\Delta\tau \leq 0.07$. At this optical depth sensitivity, we would be able to detect (at $\geq 5\sigma$ significance) CO and HCO+ column densities of $N_{CO} = 2.8 \times 10^{15}$ cm^{-2} and $N_{HCO^+} = 3.4 \times 10^{12}$ cm^{-2}. These correspond to molecular hydrogen column densities of $N_{H_2} = 9.3 \times 10^{20}$ cm^{-2} and $N_{CO} = 1.7 \times 10^{21}$ cm^{-2}, using the Galactic conversion factors $N_{HCO+}/N_{H2} = 2 \times 10^{-9}$ and $N_{CO}/N_{H2} = 3 \times 10^{-6}$ (Liszt & Lucas, 2000a; Burgh et al., 2007). All known redshifted CO/HCO+ absorption lines would be easily detected at our target sensitivity.

We based our observing time requirements on the sensitivities at the upper edges of the Ka- and Q-bands, as the sensitivities are lowest here. Using the VLA Exposure Calculator we found that an RMS noise of 6.6 mJy per 10 km/s (i.e. 1.5 MHz at 48 GHz and 1 MHz at 33 GHz) channel can be achieved with 1 min. of on-source Ka-band time at 40 GHz, and 2 min. of Q-band time at 48 GHz, in average winter conditions, at medium elevations, with two polarizations and natural weighting. Of course, the RMS noise sensitivities at the lower parts of each band will be superior to this, by about a factor of 2. We thus observed for 2 min. per source at Q-band and 1 min. at Ka-band, i.e. on-source times of 19.5 hours at Q-band and 9.75 hours at Ka-band.

We maximised the efficiency of observations by using the fact that all target source were point sources (unresolved by the VLA). Since all the sources are point sources, and therefore phase calibrators themselves, we did not do a separate phase calibration. Also, since we are aiming to simply detect absorption lines (with VLA follow-up for an accurate measurement of the optical depth), we did not do a separate flux calibration. No distinct bandpass calibration was performed; the two brightest sources of each group were used as bandpass calibrators for the group.

The largest overheads in observing times came due to the slewing times for the large number of sources. The sources were grouped by position on the sky, with the

pointing determined every hour on a strong nearby source. The groups were made up of as many as 43, and as few as 10 sources, depending on the minimization of the total time taken. All of these factors gave the observations a high observing efficiency, and only ~ 50 hours were needed for the full survey. All observations were completed in June 2013.

Unfortunately, one of the VLA scheduling blocks could not be completed during the observing cycle, due to scheduling problems. As a result, only 549 sources were observed, out of the full sample of 585. This has no effect on the statistical completeness of the sample as there was no flux density bias in the exclusion of these sources.

Chapter 4

Data Analysis

A total of 549 sources were observed in 17 days of observations with the VLA Ka- and Q- bands, with most of them using the most compact configuration, the VLA D-array. The initial data analysis was performed using the Astronomical Image Processing System (AIPS) of the National Radio Astronomy Observatory. The complete raw data volume was ~ 2.3 Terabytes, with each data set ranging from 50 to 150 Gigabytes. Each day's observations contained 10-40 sources.

The book-keeping was a critical aspect, as each of the Ka- and Q-bands is divided into four 2 GHz bands by IF filters, and each 2 GHz IF band is further sub-divided into sixteen 128 MHz sub-bands, using digital filters in the WIDAR correlator. Each 128 MHz sub-band had 128 channels, yielding a frequency resolution (i.e. channel width) of 1 MHz. So the spectrum for each source consisted of 8192 channels, which included overlaps between adjacent 2 GHz IF bands.

4.1 Initial analysis in AIPS

As per the observing strategies explained previously, no separate bandpass, flux, or phase calibrators were observed. The strongest source observed in each observing run was used to calibrate the shape of the bandpass for all the other sources, while the second-strongest source was used for bandpass calibration for the strongest source. In some cases, multiple secondary bandpass calibrators had to be used to calibrate the bandpass of the strongest source. No separate flux calibrator was observed, and a flux density of 1 Jy was assumed for all sources. No imaging was done as all sources are point sources, unresolved by the VLA. Since a point source at the phase centre of an interferometer beam can be used as a phase calibrator in its own right, no separate phase calibrator was observed. The initial data analysis, including all data editing and calibration, was carried out in AIPS. In general, the following approach was taken for the analysis of the visibility data:

1. FRING was used to to fix any improperly set antenna delays

2. BPASS was used to obtain the bandpass shapes. The bandpass was normalised by division by channel-0. Phase calibration was determined and applied before determining the bandpass, because of the short timescale of variation at these high observing frequencies. This was performed assuming a point-source model, on short timescales of $\sim 9sec$.

3. CALIB was used to calculate the antenna-based gains for all the sources after applying the bandpass. Amplitude and phase calibration was performed with an assumed flux density of 1 Jy and assuming all sources to be point sources at the phase centre. Typically, the solutions were determined at short time intervals of 0.15 minutes ($\sim 9sec$). For weaker sources, this time was increased. For the weakest sources, 2 minute intervals were used. If good solutions could not be determined for the antenna gains even after this, the sources were flagged.

4. UVLIN was used to fit and subtract a linear baseline to each 128 MHz sub-band, after applying the flagging and calibration. This task does a fit to the visibility spectra on a baseline-by-baseline basis, and the fit was determined using the channels 3-126 in each sub-band.

At each step, POSSM was used to inspect the data and UVFLG to flag any dead antennas or IFs. Some flagging was needed due to problems with individual antennas, IFs (possible correlator failures) and RFI, which was rare at these high frequencies.

For each source, the spectra were obtained by vector averaging of visibilities after calibration and flagging. These were converted to optical depth units, using the equation

$$\tau = -log(\frac{I}{I_0}) \tag{4.1}$$

where I is the measured flux density and I_0 is the flux density of the background source (normalized to unity), and τ is the optical depth of the spectrum. The sources are compact at millimetre wavelengths and so we implicitly assume that any foreground absorber entirely covers the background source, i.e. a covering factor of unity.

The rest of the analysis – the noise estimates, and the search for features – was performed using the optical depth spectra. Each 128 MHz digital sub-band for each source was treated as an independent spectrum in all the steps. Due to various problems with the data, only 501 sources of the full sample could be analysed in the present project.

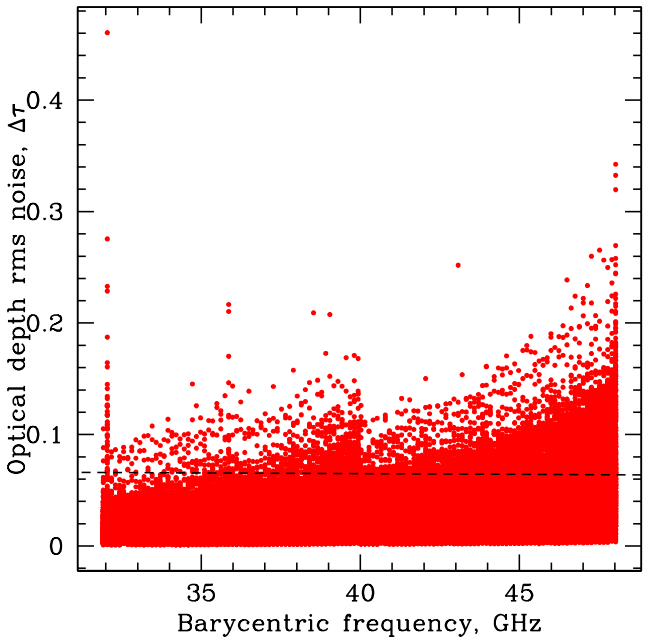

Figure 4.1: Central RMS noise for each IF band as a function of frequency, for all sources: It can be seen that the RMS noise increases steadily with frequency, from 32 to 40 GHz, and from 40 GHz to 48 GHz

4.2 Noise Estimates

Before searching for significant features, getting accurate representations of the noise spectrum was critical. The noise increases at the edges of the four 2 GHz bands, as well as at the edge channels of each of the 64 IF sub-bands. Initially, the root-mean-square (RMS) noise was calculated using the central 108 channels, for each IF sub-band, for each source. As can be seen from Fig. 4.1, the central RMS noise is a strong function of the observing frequency; it increases from 32 - 40 GHz, and then again from 40 - 48 GHz (i.e. from the lower to the upper ends of the Ka- and Q-bands). The RMS noise was calculated over the central 108 channels because this was the largest channel range over which the bandpass was flat to within $\sim 5\%$, as can be seen in Fig. 4.2.

Since the 2 GHz IF bands taper off at the edges, the digital sub-bands at the beginning and ends of these bands have an additional roll-off, in addition to the the shape of the digital filters. For example, it can be seen from Fig. 4.2 that there are clear slopes at the lower and upper edges in the bandpasses for sub-bands 1 and 64, respectively, while the bandpass is relatively flat (within $\sim 5\%$) over the channel range 11-118 for sub-band 25. Therefore, the channel range 11-118 was used for

the computation of the RMS noise for all bands other than the eight sub-bands at the start and end of the four 2 GHz IF bands. Smaller ranges – channels 17-118 for the sub-bands 1,17,33,49, and channels 12-100 for the sub-bands 16,32,48 and 64 – were used for the edge sub-bands.

For each 128-channel spectrum, we then divided the central RMS noise by the shape of the average normalized bandpass to determine the RMS noise at each channel. This was done because the RMS noise obviously increases at the edges of each sub-band, due to the shape of the digital filter. Using the estimate of the RMS noise from the central channels at the edges would result in an under-estimate of the RMS noise, and thus an incorrect estimate of the statistical significance of putative features. Finally, we chose to flag out the two channels at the start and end of each 128-channel sub-band, as the bandpass is poorly determined at these edges, and the noise estimates are thus unreliable. This implied that we flagged $\sim$ 3% of the data.

Furthermore, since we know that the noise is not well represented by the bandpass shape at the upper end of IF sub-bands 16, 32, 48 and 64, and at the lower end of IF sub-bands 1, 17, 33 and 49, we checked whether the number of 3σ features in these IF sub-bands showed an specific dependence on the channel number. It was seen that the number of features was significantly larger in the channel range $106 - 126$ for IF sub-bands 16, 32, 48, and 64, and similarly for channels $1 - 8$ for IF sub-bands 1, 17, 33 and 49. We hence flagged these channel ranges for these specific IF sub-bands. This removed $\sim 1\%$ of the data.

Since it is known that temporal variations in the bandpass shape can result in residual curvature in the final spectrum, we attempted to remove such residual curvature in the spectrum by fitting a low-order polynomial to each 128-MHz spectrum, restricting to channels 3-126 and making use of the RMS noise spectra. First and second order fits were generated for each of the spectra, and a baseline was subtracted in those cases where the fit was needed. Fit parameters as well as the uncertainty on these parameters were calculated using the package GNUPLOT, which weighted the spectra using the noise spectrum provided. Only those fits were subtracted which had *significant* fit parameters, i.e. the uncertainty on the parameters $\leq 33\%$.

4.3 Tests for Gaussianity

The search for significant features is based on the assumption that all of the spectra are Gaussian in nature. We verified this by using two standard statistical tests, the Kolmogorov-Smirnov (K-S) test and the Anderson-Darling (A-D) test. The A-D test is known to have fewer biases than the K-S test, and serves as a better discriminator against non-Gaussianity, but since both the tests suffer from

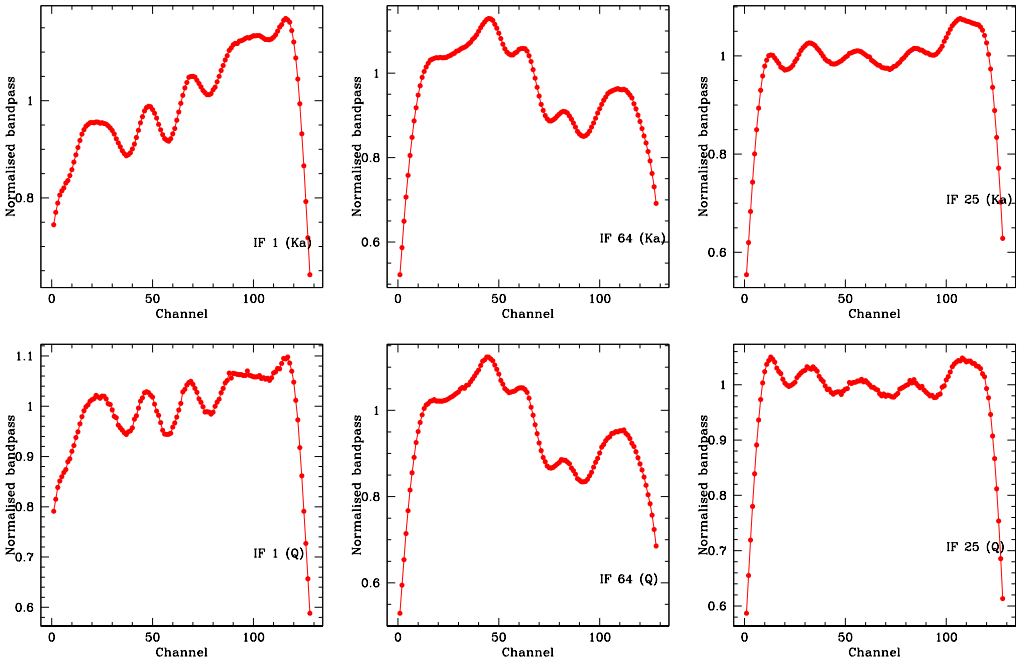

Figure 4.2: IF-1, IF-64, and IF-25 for the Ka- and Q- band data: It can be seen that the bandpass shapes taper off in the IF-1 and IF-64 sub-bands towards lower and higher frequencies respectively, whereas they remain relatively flat for the IF-25 sub-band, in both the Ka- and Q- bands.

different biases, both of them were used. We tested each sub-band for each source using the K-S and the A-D tests. Sub-bands that returned a p-value $< 10^{-6}$ in either of the two tests were flagged out.

The p-value threshold was determined based on simulations of Gaussian spectra. A set of spectra, 10 times our sample size, was generated. It was checked at what p-value fewer than 10 of those spectra were failing our tests. At this p-value, we would have flagged ≤ 1 spectrum that was genuinely noise-like, since our sample was 10 timer smaller than the simulated sample. A p-value of 10^{-6} was found to be an appropriate choice for our data set. After applying the above tests, 0.04% of the data were flagged.

It is possible that a spectrum might fail the tests of Gaussianity if it contains strong (and real) absorption features. This was evidenced by the fact that the spectra from PKS1830-211 which included the strongest(known) absorption features were flagged out by the above procedure. Hence, all spectra flagged by the above tests of Gaussianity were visually inspected to ensure that the low p-value was not due to the presence of strong spectral features. Further, to test whether the presence of strong features might yield a low p-value, the A-D and K-S tests

were re-run on spectra with low p-values after discarding the channels with values most discrepant from zero. If the p-value then showed a significant improvement, it was clear that the earlier low p-value was simply due to the presence of the spectral feature and the sub-band was then unflagged.

4.4 Statistically significant features

After all flagging and baseline subtraction, the final optical depth spectra for each 128-MHz sub-band were searched for spectral features at different levels of statistical significance, using the RMS noise spectra described in Section 4.1. Features that occurred at the same frequency in different sources were eliminated; this is an indication of RFI, especially if these sources were observed on the same day.

In order to identify systematics in the data or the analysis procedure, we checked whether the distribution of features was uniform across frequencies, channels, and across different IFs, as well as across the different days of observations. Since the number of features with $\geq 3\sigma$ significance is expected to be very large, based on Gaussian noise statistics, and is unlikely to be affected by the presence of real features, we studied the distribution of such features to identify possible biases. We found that the number of features with $\geq 3\sigma$ significance was not correlated with the channel number or the IF number. For example, Fig. 4.3 shows the number of such features plotted against channel number, for all IF sub-bands; it is clear that the number is roughly constant across the channel range 3-126, and does not depend on channel number. Similarly, no systematic effect was found in the distribution of features with regard to IF sub-band, in either the Ka- or the Q-band.

Note: In the original version of this thesis, we had used the channel range 20-110 in UVLIN. This yielded a uniform distribution of features with $\geq 3\sigma$ significance in the channel range 20-110, but a higher number of such features in the channel ranges 3-20 and 111-126. This problem apparently arises due to an issue inside the UVLIN code, for reasons that are not clear. We hence chose to use the channel range 3-126 in UVLIN in the final analysis, and have updated our results to reflect the resulting changes.

Within the channel range 3-126, significant features were searched for in both emission and absorption. Excluding the source PKS1830-211, we found 36 features at $\geq 5\sigma$ statistical significance in absorption, and 17 features at $\geq 5\sigma$ significance in emission. These included 1 features at $\geq 6\sigma$ significance and 3 features at $\geq 6\sigma$ significance, in absorption and emission respectively. A number of feature have been detected towards the source PKS1830-211. Some of the detected absorption lines from PKS1830-211, and some of the tentative features have been shown in Figs. 4.5-4.7.

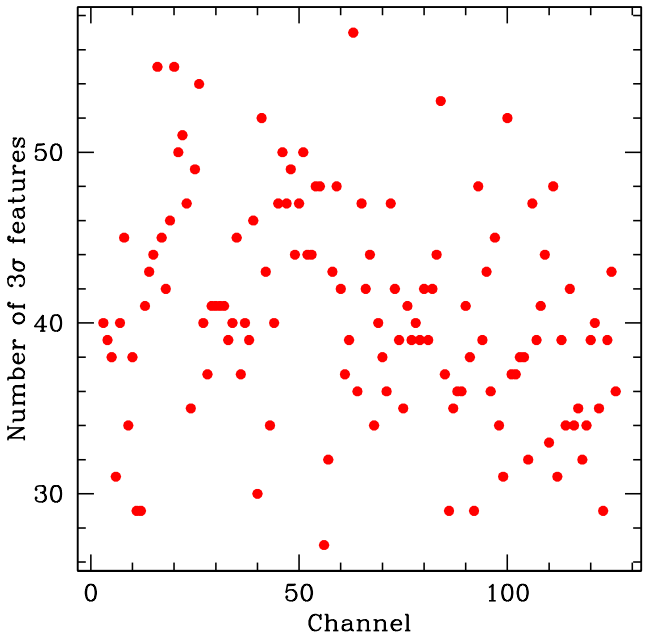

Figure 4.3: Distribution of 3σ features as a function of channel number

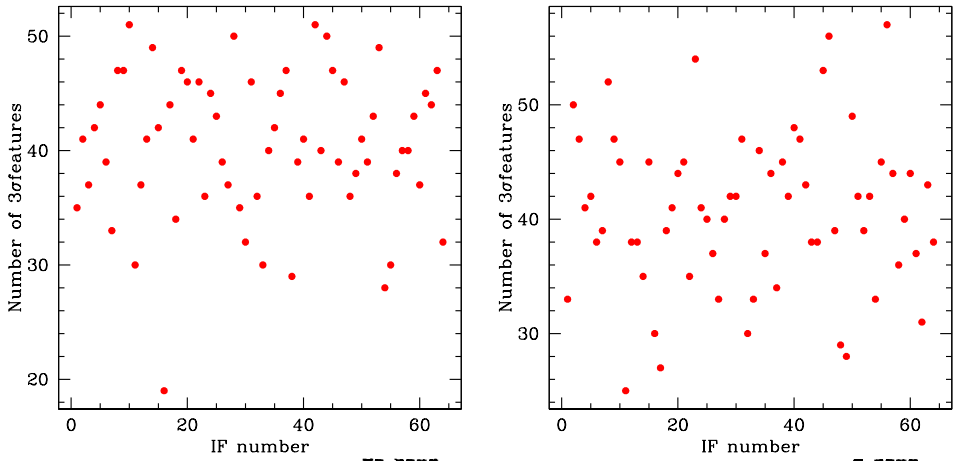

Figure 4.4: Distribution of features as a function of IF sub-band in (a) Ka- band and (b) Q- band

4.5 Total Redshift Path

To quantify the number density of molecular absorbers as a function of redshift, we need to calculate the total redshift path. Since a total of 12.5 % of the data has

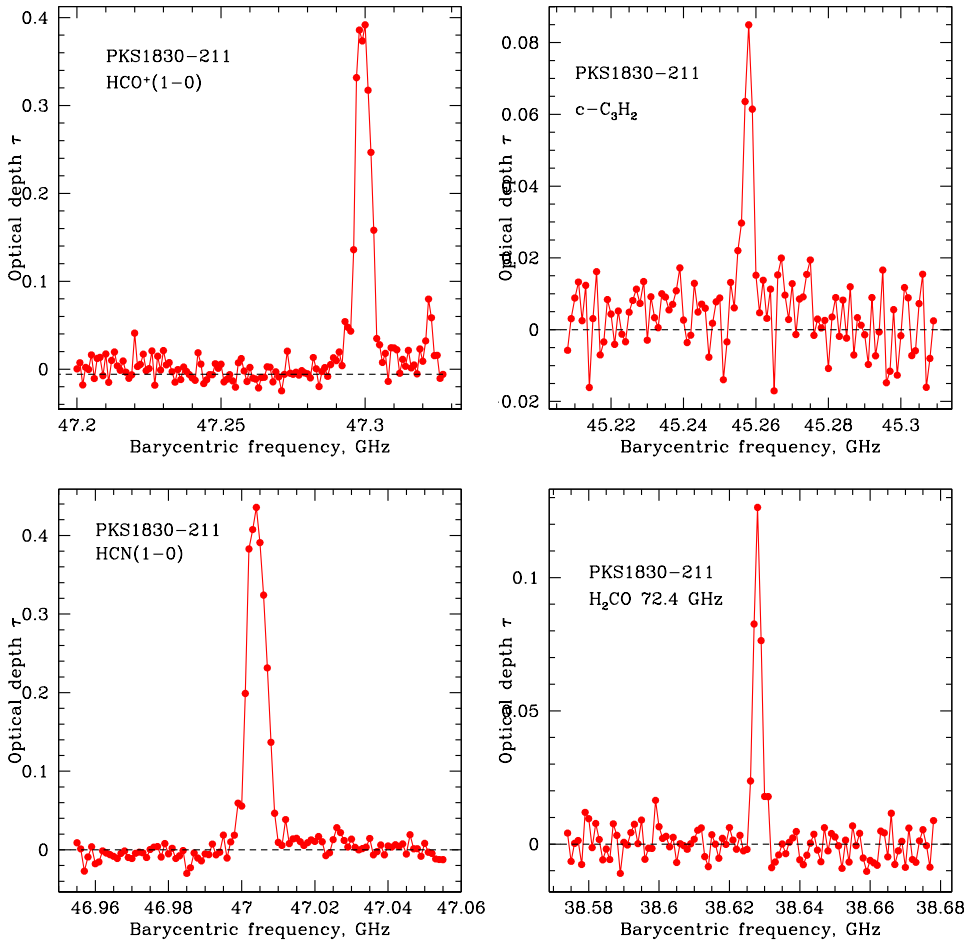

Figure 4.5: Features at $\geq 5\sigma$ significance detected at $z = 0.88582$ towards PKS1830-211.

been flagged, there are "holes" in the frequency coverage that need to be taken into account. We are considering three molecular transitions, HCO^+(1-0), CO(1-0) and HCO^+(2-1). For each transition frequency, it is possible to make a mapping from frequency space to redshift space using $\nu_0/\nu = 1 + z$, where ν is the observation frequency, ν_0 is the rest frequency of the transition, and z is the redshift. Using this map between frequency and redshift, if we know which channels have been flagged, we can directly find out which redshift range is not covered.

Also, the redshift coverage of the CO(1-0) line is $1.4 < z < 2.6$ and for the HCO^+(1-0) line is $0.9 < z < 1.8$; they overlap in the redshift range $1.4 < z < 1.8$. This corresponds to a frequency range of 31.856 GHz to 37.212 GHz for HCO^+(1-0), and a frequency range of 41.2 GHz to 48.095 GHz for CO(1-0). So if channels

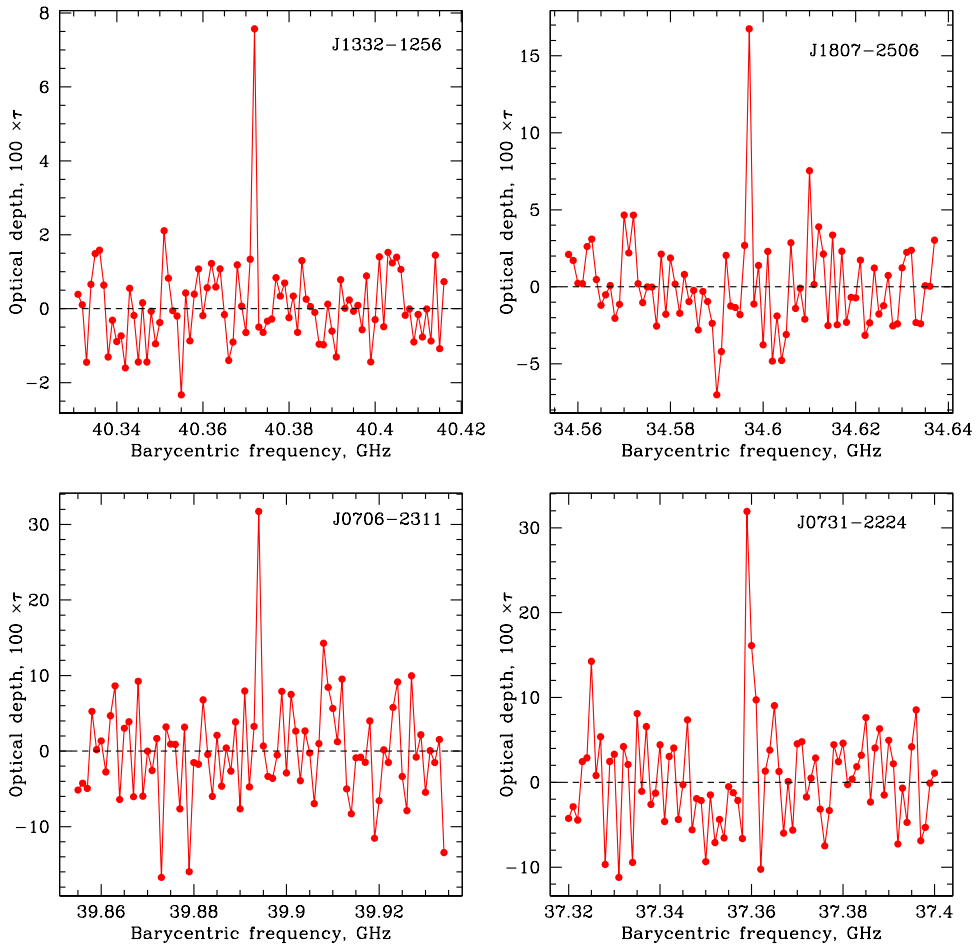

Figure 4.6: Examples of features detected in the survey at $\geq 5\sigma$ significance.

are flagged in one of the frequency ranges, it is possible to save the redshift path if the corresponding frequency channels in the other band have not been flagged out. Since the higher frequency Q-band channels are much more likely to be flagged due to low sensitivity, while the channels in the Ka band are very rarely flagged, the loss of redshift path was mitigated. Next, each of the four 2 GHz IF bands, as well as the Ka and Q bands, overlapped to some extent at the edges. These were removed before the calculations of the redshift path. After taking all the above into consideration, we have a final redshift path of $\Delta z = 188.2$, with a median redshift of $z = 1.5$.

Fig. 4.7 shows the redshift path density $g(z)$ as a function of the redshift. It can be seen that $g(z)$ peaks close to $z = 1$; this is because the redshift $z = 1$ was the cutoff in the selection of the target sources. The path density decreases as

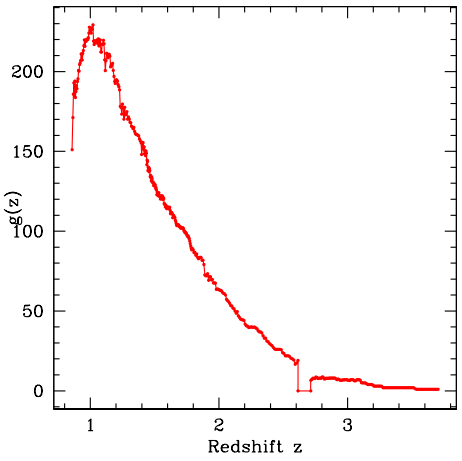

Figure 4.7: The redshift path density $g(z)$ as a function of redshift z.

a function of z; this is because the number of sources decreases with increasing redshift. The function $g(z)$ goes to zero in the redshift range $2.6 < z < 2.7$; this is because this redshift range is not covered in any of the transitions.

4.6 Final data sample

We have analysed the VLA Ka- and Q- band spectra of 501 source spectra in Ka and Q bands, with each source spectrum sub-divided into 64 spectra from the WIDAR digital sub-bands. We have flagged 12.5% of these data. A very small fraction, 0.04 % of the data, has been flagged because of spectra failing the K-S or A-D tests. Of the 501 sources, 245 have known redshifts, and 256 sources do not. We get a total redshift path of $\Delta z = 188.2$, with a median redshift of $z = 1.5$ at the optical depth RMS noise threshold $\Delta\tau \leq 0.07$.

Chapter 5

Results and Discussion

5.1 Survey Statistics

We have analysed the data for 501 sources in this study, 245 of which have known redshifts. We have flagged 12.5% of the data in all. We have a final redshift path of $\Delta z = 188.2$ at the optical depth RMS noise limit $\Delta\tau \leq 0.07$, calculated using the 245 sources with known redshifts.

We carried out a search for statistically significant features, at different levels of significance, in all 64 sub-bands for each of the 501 sources, at the original velocity resolution. The channels that have a noise greater than 0.07 have been flagged for the calculation of the redshift path, but have still been searched for signficnt features. We have 7944112 independent channels which we have searched. According to Gaussian statistics, we expect to see a total of four features at $\geq 5\sigma$ significance - two in emission and two in absorption. After searching all the spectra, and eliminating those features that occurred at the same frequency in different sources, we have found 36 absorption features and 17 emission features at $\geq 5\sigma$ significance (excluding features towards the source PKS1830-211)

Of these, four features (1 in absorption and 3 in emission) have $\geq 6\sigma$ significance. All the strong features arising from the known molecular absorber at $z = 0.88582$ towards PKS1830-211 will henceforth be counted as a single absorption system. Excluding PKS1830-211, the 36 absorption features with $\geq 5\sigma$ significance arise towards 30 sources; multiple such features were detected towards the same source. In emission, there are 17 features arising towards 13 sources.

The number of detected features is not necessarily the same as the number of absorbers; a single absorber can produce multiple strong absorption features in the observing frequency range 32-48 GHz, from the CO (1-0), HCO^+(1-0), HCN (1-0), HNC (1-0) lines. For example,multiple transitions have been detected at high significance at the same redshift towards PKS1830-211, i.e. they are produced by

a single absorber.

In the estimate of the redshift number density, the number of absorbing systems is to be used, and not the number of features. However, we have been unable to identify the transition lines and determine if they are from the same redshift i.e. from the same source, and hence will assume that they arise from different redshifts. The only exception to this is for the features towards PKS1830-211, which are known to arise in a single absorber, and which will hence be counted as a single system. Therefore, we have a total of 37 candidate absorbers detected at $\geq 5\sigma$ significance.

Any detected emission features in such a shallow survey are unlikely to be real, as they would imply an extremely large molecular gas mass, and would be unlikely to produce lines with narrow velocity widths. There are also no strong Galactic emission lines that are likely to be detectable at our observing frequencies, at our sensitivity. For example, CS 1-0 is at 48.9 GHz, outside the band; there are CH_3CN and HC_3N lines in the observing band, but these would be expected only from large Galactic molecular clouds. We would thus expect only as many strong emission features as should arise from Gaussian noise. An equal number of such features would be seen in both emission and absorption. If the number of features seen in absorption is significantly larger than that seen in emission, then at least some of them are likely to be real.

We can therefore conclude that the emission features are unlikely to be real and can hence be used as a probe of unknown systematic effects. Since we know that the emission features are unlikely to be real, and since the number of emission features is not consistent with Gaussian statistics, it is likely that unknown systematic effects are responsible for the features found in emission. There is no reason to assume that these systematic effects would only give rise to emission features. As such, one would expect a comparable number of absorption features from similar systematic effects. It is thus possible that ≈ 17 of the detected absorption features also arise due to the above unknown systematic effects. Since there are a total of 37 absorption features, we conclude that $20^{+5.55}_{-4.43}$ are likely to be real, where the above errors are for small number statistics(Gehrels, 1986).

We can quantify the abundance of molecular clouds at high redshift by calculating the redshift number density, $n(z)$, which we define as,

$$n(z) = \frac{N}{\Delta z} \tag{5.1}$$

where N is the number of molecular absorbers detected, and $\Delta z = 188.2$ is the total redshift path. We can calculate the redshift number densities assuming the two extreme cases, (i) that all the excess,$20^{+5.55}_{-4.43}$, absorption features with $\geq 5\sigma$ significance are real, and (ii) that only one system showing absorption is real, that at $z = 0.88582$ towards PKS1830-211. These will give us upper and lower bounds

on the redshift number density of molecular absorbers.

Assuming case (i) above, that the excess $20^{+5.55}_{-4.43}$ absorption features are real, we obtain a redshift number density $n(z) = 0.106^{+0.029}_{-0.024}$. Conversely, for case (ii), if the only real absorber is that at $z = 0.88582$ towards PKS1830-211, the total number of absorbers is $N = 1^{+2.30}_{-0.827}$, yielding a redshift number density $n(z) = 0.005^{+0.012}_{-0.004}$.

5.2 Discussion

Our threshold sensitivity, $\Delta\tau \leq 0.07$, implies that CO and HCO^+ column densities of $N_{CO} = 2.8 \times 10^{15}$ cm^{-2} and $N_{HCO^+} = 3.4 \times 10^{12}$ cm^{-2} would have been detected at 5σ significance, assuming an excitation temperature of $T_{ex} = 10$ K. We shall assume that the Galactic conversion factors are $N_{CO} \sim 3 \times 10^{-6} N_{H_2}$ (which is valid for diffuse/translucent clouds (Burgh et al., 2007) and $N_{HCO^+} \sim 2 \times 10^{-9} N_{H_2}$ (Liszt & Lucas, 2000a,b), and that these are valid at high redshifts. Our CO-H_2 conversion factor is the the median value of the ratio N(CO)/N(H_2) obtained by (Burgh et al., 2007) for diffuse clouds; dark clouds are likely to have higher ratios, $\sim 2 - 3 \times 10^4$(Lacy et al., 1994). Using these conversion factors, we conclude that H_2 column densities $\geq 1.7 \times 10^{21}$ cm^{-2} would have been detected at $\geq 5\sigma$ significance in the survey, either in the CO or the HCO^+ transitions. We note that the above sensitivities to the H_2 column density are conservative as we have used the lower CO-to-H_2 conversion factor.

We have a total redshift path of $\Delta z = 188.2$. Our upper bound on the redshift number density of molecular absorbers with H_2 column densities $\geq 1.7 \times 10^{21}$ cm^{-2} is $n(z) = 0.106^{+0.029}_{-0.024}$.

In the first large scale blind survey for molecular absorption, which was conducted using the GBT by Kanekar et al. (2014), they had a total redshift path of $\Delta z = 23.2$, with an optical depth RMS noise threshold of $\Delta\tau \leq 0.125$. They obtained a 2σ upper limit of $n(z = 1.2) < 0.15$ to the redshift number density, at the above RMS noise threshold. The present VLA survey is a factor of 8 better in total redshift path than the GBT survey, and the numbers are hence much more statistically reliable. Of course, the lack of detections in the much smaller redshift path of Kanekar et al (2014) is entirely consistent with the low redshift number densities obtained here.

It is interesting to compare the redshift number density of atomic absorption, using damped Lyman-α surveys, with the redshift number densities obtained in this work for molecular gas. There have been two surveys for DLA absorption using radio-selected target source samples: the CORALS and the USCD surveys(Ellison et al., 2001; Jorgenson et al., 2006). These were sensitive to absorbers at higher redshifts, at $z \geq 2$, and had total redshift paths of $\Delta z \approx 55$ and $\Delta z \approx 41$. Our redshift path is significantly larger than the combined CORALS

and UCSD surveys, but comparisions are difficult since our median redshift is $z = 1.5$.

Surveys for DLAs at lower redshifts, $z < 1.7$ Rao et al. (2006), have so far not been carried out on radio-selected samples and are thus likely to suffer from dust bias. In addition, Rao et al. (2006) selected targets based on the presence of strong MgII absorption, introducing additional systematics which are difficult to quantify (e.g. Kanekar et al., 2014). However, their $n(z)$ estimate at $z \sim 1.2$ is consistent with the value obtained at $z \sim 2.2$ from the much larger (but again, optically-selected) DLA surveys with the Sloan Digital Sky Survey (Noterdaeme et al., 2012), suggesting that the redshift number density of DLAs does not evolve significantly over the redshift range $2.2 - 1.2$. We will hence compare our estimate of the redshift number density of molecular absorbers at $z \sim 1.5$ to the DLA number density estimates of Rao et al. (2006), to estimate the relative spatial extents of atomic and molecular gas in high-z galaxies. Rao et al. (2006) obtained $n_{\rm DLA}(z = 1.219) = 0.120 \pm 0.025$ for the redshift number density of DLAs, while we obtain $0.005 \leq n_{\rm H_2}(z = 1.5) \leq 0.11$. We thus find that the ratio of redshift number densities in atomic and molecular gas $f \equiv n_{\rm DLA}/n_{\rm H_2} = 1.1 \leq f \leq 24$. If we assume that the atomic and molecular gas in galaxies at $z \approx 1.5$ is distributed in a rotating disk, as is the case in local spiral galaxies, this would imply that the relative transverse sizes of the atomic and molecular gas distributions must be $1 < s_{\rm HI}/s_{\rm H_2} < 4.9$, where s_{HI} and s_{H_2} are the transverse sizes of the atomic and molecular disks, respectively. This is the first-ever estimate of the spatial extent of molecular gas in normal galaxies at high redshifts.

Chapter 6

Summary and future work

6.1 Summary

We have observed a total of 549 sources from the initial sample of 585 sources; due to time constraints on the VLA, a set of 36 sources was not observed. 48 additional sources were removed due to calibration problems or because of low flux densities; we plan to analyse these sources later. We herefore have a final sample of 501 sources. These were observed with the Ka- and Q-bands of the VLA and the WIDAR correlator; the observations used sixty four 128-MHz IF sub-bands to obtain uniform coverage of the frequency range 32-48 GHz with a spectral resolution of 1 MHz (i.e. a velocity resolution of 6-9 km/s). The frequency coverage corresponds to the redshift range $0.85 < z < 2.6$ in the HCO^+ (1-0) and CO (1-0) lines, and the redshift range $2.72 < z < 4.57$ in the HCO^+ (2-1) line.

The initial data analysis, including data editing, gain and bandpass calibration, and baseline subtraction, was carried out in AIPS. The 64 individual sub-band spectra for each source were then processed independently outside AIPS, using our own custom scripts. We have tested each individual 128 MHz IF spectrum for Gaussianity using the A-D as well as the K-S tests. Sub-bands whose spectra showed evidence for non-Gaussianity (selecting a p-value threshold of $< 10^{-6}$) were excluded from the analysis, and also from calculation of the redshift path. All the flagged IFs were checked and visually inspected to ensure that the low p-value was not due to an absorption feature.

For each spectrum, we have flagged the channels 1-2 and the channels 127-128. For the IF sub-bands at the beginning and end of the 2 GHz IF bands, additional edge channels were flagged. A total of $\approx 4\%$ of the data were flagged in this manner. Additionally, the channels with an optical depth RMS noise ≥ 0.07 were flagged for the redshift computation, though they were searched for the presence

of significant features. Finally, 12.5% of the data were flagged from the redshift path calculation, due to either low sensitivity, RFI or edge effects.

245 of the 501 sources had known redshifts from the literature, in the range $1.0 < z < 3.2$. For each of these, we computed the redshift path covered by the survey in the HCO^+ (1-0), CO (1-0), and HCO^+ (2-1) absorption lines, by summing the covered redshift ranges (out to the source redshift and excluding any flagged channels) with RMS optical depth noise ≤ 0.07 i.e. meeting our target optical depth threshold limit. Further summing over all sources with known redshifts, we obtain a total redshift path of $\Delta z = 188.2$. This is a factor of ~ 8 higher than the redshift path of the sole earlier blind survey for molecular absorption, with the GBT (Kanekar et al., 2014). Our survey also has a better sensitivity than the GBT survey, by a factor of ~ 1.7.

This optical depth RMS noise limit corresponds to the column densities of $N_{CO} = 2.8 \times 10^{15}$ cm^{-2} and $N_{HCO^+} = 3.4 \times 10^{12}$ cm^{-2}. Assuming the Galactic conversion factors, H_2 column densities of $N_{H_2} \geq 1.7 \times 10^{21}$ cm^{-2} would be detected at $\geq 5\sigma$ sigificance.

We have searched for statistically significant features at the original velocity resolution, ranging from 6.4 km/s at 48 GHz to 9.2 km/s at 32 GHz. These resolutions are well-matched to the expected velocity spread of molecular absorption features, ~ 10 km/s.

At this resolution, we have found 36 features at $\geq 5\sigma$ significance in absorption, and 17 features at $\geq 5\sigma$ significance in emission. Only one of the significant features in absorption is detected at $\geq 6\sigma$ significance. Features arising from the single absorber at $z = 0.88582$ towards PKS1830-211 have not been included in these numbers.

Based on the above analysis, we obtain a redshift number density of molecular absorbers $0.005 \leq n(z = 1.5) \leq 0.11$, with a survey redshift path $\Delta z = 188.2$, a factor of ≈ 8 larger than the redshift path of the largest earlier blind survey for molecular absorption (Kanekar et al., 2014).

Comparing these bounds with the redshift number density of DLAs, we have obtained $1 \leq s_{\rm HI}/s_{\rm H_2} \leq 4.9$, where s_{HI} and s_{H_2} are the transverse sizes of the atomic and molecular disks. This is the first comparision between the spatial extent of molecular and atomic gas at high redshifts.

6.2 Future Work

The first step is to complete the analysis of the remaining 48 sources that had technical problems with the calibration and were excluded from the present analysis, and obtain all the data that can be used for this study. These sources may include extended sources, some of which will violate the assumption of a point source at

phase centre in the calibration; imaging and detailed self-calibration procedures may be necessary for these sources. Another systematic effect that must be understood is why the number of features seen in emission is not consistent with Gaussian statistics.

Once the remaining 48 sources have been analysed, we shall have a comprehensive list of putative absorption features, which will then be confirmed or denied using deeper follow-up observations with the VLA.

References

Burgh E. B., France K., McCandliss S. R., 2007, ApJ, 658, 446

Carilli C. L., Menten K. M., Reid M. J., Rupen M. P., 1997, ApJ, 474, L89

Carilli C. L., Perlman E. S., Stocke J. T., 1992, ApJ, 400, L13

Carilli C. L., Walter F., 2013, ARA&A, 51, 106

Combes F., Wiklind T., 1997, ApJ, 486, L79

Combes F., Wiklind T., Nakai N., 1997, A&A, 327, L17

Drinkwater M. J., Webb J. K., Barrow J. D., Flambaum V. V., 1998, MNRAS, 295, 457

Ellison S. L., Yan L., Hook I. M., Pettini M., Wall J. V., Shaver P., 2001, A&A, 379, 393

Gehrels N., 1986, ApJ, 303, 336

Jorgenson R. A., Wolfe A. M., Prochaska J. X., Lu L., Howk J. C., Cooke J., Gawiser E., Gelino D. M., 2006, ApJ, 646, 730

Kanekar N., 2011, ApJ, 728, L12

Kanekar N., Briggs F. H., 2003, A&A, 412, L29

Kanekar N., Carilli C. L., Langston G. I., Rocha G., Combes F., Subrahmanyan R., Stocke J. T., Menten K. M., Briggs F. H., Wiklind T., 2005, Phys. Rev. Lett., 95, 261301

Kanekar N., Chengalur J. N., 2002, A&A, 381, L73

Kanekar N., Chengalur J. N., 2008, MNRAS, 384, L6

Kanekar N., Chengalur J. N., Ghosh T., 2004, Physical Review Letters, 93, 051302

Kanekar N., Gupta A., Carilli C. L., Stocke J. T., Willett K. W., 2014, ApJ, 782, 56

Kühr H., Witzel A., Pauliny-Toth I. I. K., Nauber U., 1981, A&AS, 45, 367

Lacy J. H., Knacke R., Geballe T. R., Tokunaga A. T., 1994, ApJL, 428, L68

Lanzetta K. M., McMahon R. G., Wolfe A. M., Turnshek D. A., Hazard C., Lu L., 1991, ApJS, 77, 1

Ledoux C., Petitjean P., Srianand R., 2003, MNRAS, 346, 209

Liszt H., Lucas R., 2000a, A&A, 355, 333

Liszt H., Lucas R., 2000b, A&A, 355, 333

Muller S., Beelen A., Black J. H., Curran S. J., Horellou C., Aalto S., Combes F., Guélin M., Henkel C., 2013, A&A, 551, 109

Muller S., Beelen A., Guélin M., Aalto S., Black J. H., Combes F., Curran S. J., Theule P., Longmore S. N., 2011, A&A, 535, 103

Murphy M. T., Webb J. K., Flambaum V. V., 2003, MNRAS, 345, 609

Murphy M. T., Webb J. K., Flambaum V. V., Drinkwater M. J., Combes F., Wiklind T., 2001, MNRAS, 327, 1244

Murphy T., et al., 2010, MNRAS, 402, 2403

Noterdaeme P., Laursen P., Petitjean P., Vergani S. D., Maureira M.-J., Ledoux C., Fynbo J. P. U., López S., Srianand R., 2012, A&A, 540, 63

Noterdaeme P., Ledoux C., Petitjean P., Srianand R., 2008, A&A, 481, 327

Rao S. M., Turnshek D. A., Nestor D. B., 2006, ApJ, 636, 610

Riechers D. A., Carilli C. L., Walter F., Momjian E., 2010, ApJ, 724, L153

Wiklind T., Combes F., 1994, A&A, 286, L9

Wiklind T., Combes F., 1995, A&A, 299, 382

Wiklind T., Combes F., 1996a, A&A, 315, 86

Wiklind T., Combes F., 1996b, Nature, 379, 139

Wiklind T., Combes F., 1997, A&A, 328, 48

Winn J. N., Kochanek C. S., Keeton C. R., Lovell J. E. J., 2003, ApJ, 590, 26

Winn J. N., Lovell J. E. J., Chen H., Fletcher A. B., Hewitt J. N., Patnaik A. R., Schechter P. L., 2002, ApJ, 564, 143

Wolfe A. M., Gawiser E., Prochaska J. X., 2005, ARA&A, 43, 861

Wolfe A. M., Turnshek D. A., Smith H. E., Cohen R. D., 1986, ApJS, 61, 249

York T., Jackson N., Browne I. W. A., Wucknitz O., Skelton J. E., 2005, MNRAS, 357, 124